Article

# Measuring phonon dispersion at an interface

https://doi.org/10.1038/s41586-021-03971-9

Received: 8 March 2021

Accepted: 31 August 2021

Published online: 17 November 2021

Check for updates

Ruishi Qi[1,2,3,13], Ruochen Shi[1,2,13], Yuehui Li[1,2], Yuanwei Sun[1,2], Mei Wu[1,2], Ning Li[1,2,4], Jinlong Du[1], Kaihui Liu[5,6,7], Chunlin Chen[8], Ji Chen[5,6], Feng Wang[3], Dapeng Yu[1,9], En-Ge Wang[2,10,11] & Peng Gao[1,2,6,7,12] ✉

The breakdown of translational symmetry at heterointerfaces leads to the emergence of new phonon modes localized at the interface[1]. These modes have an essential role in thermal and electrical transport properties in devices, especially in miniature ones wherein the interface may dominate the entire response of the device[2]. Although related theoretical work began decades ago[1,3–5], experimental research is totally absent owing to challenges in achieving the combined spatial, momentum and spectral resolutions required to probe localized modes. Here, using the four-dimensional electron energy-loss spectroscopy technique, we directly measure both the local vibrational spectra and the interface phonon dispersion relation for an epitaxial cubic boron nitride/diamond heterointerface. In addition to bulk phonon modes, we observe modes localized at the interface and modes isolated from the interface. These features appear only within approximately one nanometre around the interface. The localized modes observed here are predicted to substantially affect the interface thermal conductance and electron mobility. Our findings provide insights into lattice dynamics at heterointerfaces, and the demonstrated experimental technique should be useful in thermal management, electrical engineering and topological phononics.

Understanding the vibrational properties of condensed-matter systems is important because phonons are involved in many physical phenomena ranging from thermal and electrical transport and superconductivity to mechanical strength and phase transition[6]. At a heterointerface, the broken translational symmetry leads to localized phonon modes[1,7], which are essential in understanding interface thermal conductance (ITC), electrical transport, structural stability and even interface superconductivity[7–11]. On the practical side, the development of various modern technologies, such as computing circuits, quantum cascade lasers and thermoelectrics, demands efficient thermal engineering of interfaces[2]. For example, ITC has become increasingly significant and even the bottleneck in heat dissipation for microelectronic devices. In contrast to the extensively used assumption that ITC can be explained by bulk phonon modes in two constituting materials, recent theoretical works have demonstrated that a large contribution from localized interfacial modes must be considered[2,7,9,12]. It is thus highly desirable to measure the dispersion relation and spatial distribution of the localized modes, which directly dictates the transport properties across the interface.

Despite their importance, related studies, especially experimental ones, are deficient. Interfacial modes have not been experimentally observed, not to mention measuring their dispersion relations. The major challenge is that they only appear in several atom layers near the interface, imposing stringent technical requirements, including nanometre spatial resolution, millielectronvolt spectral resolution, large momentum transfer and ultrahigh sensitivity. Inelastic neutron/X-ray scattering techniques are successful in bulk phonon dispersion measurements, but their beam size and sensitivity are insufficient for nanostructures[13]. Tip-enhanced optical spectroscopy has recently achieved nanometre resolution[14,15], but the tiny momentum of photons cannot access the entire Brillouin zone (BZ). Atom-surface scattering spectroscopy and high-resolution reflection electron energy-loss spectroscopy (EELS) can determine surface phonon dispersion relations[16], but their non-penetrating geometry makes interface measurements impossible.

Recent advances in scanning transmission electron microscopy (STEM) have enabled nanoscale vibrational STEM-EELS measurements in the past decade. This technique offers electron probes with high spatial, momentum and energy resolutions in conjunction with a large momentum transfer range and high detection sensitivity[17–19]. It has demonstrated its power in many nanoscale phonon measurements[17,20–29], particularly in measuring the local vibrational spectra of single

[1]Electron Microscopy Laboratory, School of Physics, Peking University, Beijing, China. [2]International Center for Quantum Materials, Peking University, Beijing, China. [3]Physics Department, University of California at Berkeley, Berkeley, CA, USA. [4]Academy for Advanced Interdisciplinary Studies, Peking University, Beijing, China. [5]State Key Laboratory for Mesoscopic Physics, School of Physics, Peking University, Beijing, China. [6]Collaborative Innovation Center of Quantum Matter, Beijing, China. [7]Interdisciplinary Institute of Light-Element Quantum Materials and Research Center for Light-Element Advanced Materials, Peking University, Beijing, China. [8]Shenyang National Laboratory for Materials Science, Institute of Metal Research, Chinese Academy of Sciences, Shenyang, China. [9]Shenzhen Institute for Quantum Science and Engineering (SIQSE), Southern University of Science and Technology, Shenzhen, China. [10]Songshan Lake Materials Lab, Institute of Physics, Chinese Academy of Sciences, Dongguan, China. [11]School of Physics, Liaoning University, Shenyang, China. [12]Beijing Graphene Institute, Beijing, China. [13]These authors contributed equally: Ruishi Qi, Ruochen Shi. ✉e-mail: p-gao@pku.edu.cn

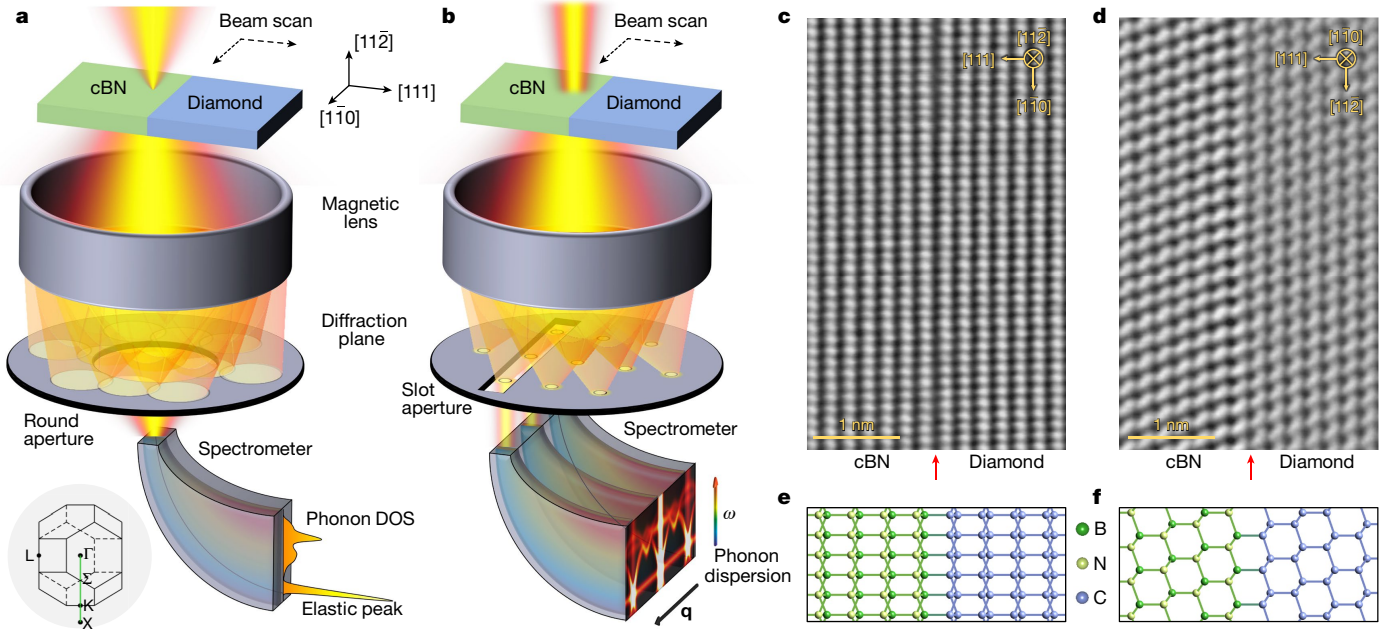


**Fig. 1 | Experimental setup and interface structure. a**, A schematic of the experimental setup (3D EELS) used to acquire the phonon DOS at atomic resolution. The inset in the bottom-left corner shows a top view of the bulk BZ with the high-symmetry points marked. The 2D interface BZ, viewed from this direction, is the vertical central line. **b**, A schematic of the experimental setup (4D EELS) used to acquire phonon dispersion curves. The slot aperture is placed parallel to the interface, producing dispersion diagrams along the high-symmetry line Γ–Σ–K–X. **c**, **d**, iDPC-STEM images of the coherent cBN/diamond interface, viewed from the [11$\bar{2}$] zone axis (**c**) and the [1$\bar{1}$0] zone axis (**d**). The red arrows mark the interface. **e**, **f**, Corresponding projections of the atomic model.

defects[25,26], and the phonon dispersion of graphene[27] and boron nitride (BN) crystals[19]. Despite the progress, owing to the intrinsic trade-off between the spatial and momentum resolutions, previous studies either achieved atomic spatial resolution upon losing momentum resolution[24,25,30] or achieved fine momentum resolution with a beam size larger than typical phonon localization scales[19,21,27,31]. Requiring both resolutions at the same time, the measurement of interface phonon dispersion has remained elusive. Here we use the recently developed four-dimensional EELS (4D EELS) technique[21] to probe the interface phonon modes at the cubic BN (cBN)/diamond heterointerface with carefully balanced spatial and momentum resolutions.

## Experimental setup

As a versatile technique, STEM-EELS can collect vibrational signals in various configurations. In general, a kiloelectronvolt electron beam is focused on the sample, launching lattice vibrations upon losing a tiny fraction of its kinetic energy. An EELS aperture on the diffraction plane selectively collects scattered electrons with desired momentum transfers. We first measure the local phonon spectra by choosing a large beam convergence angle to achieve an atomic-scale spatial resolution (Fig. 1a). A round aperture covers multiple BZs, producing spectra comparable to the local phonon density of states (DOS; although quantitatively they differ slightly[25,32]). With the beam scanning in two spatial dimensions ($x$ and $y$), a three-dimensional EELS (3D EELS; $x$–$y$–$\omega$, where $\omega$ is the frequency) dataset can be recorded. This allows us to map the spatial distribution of interfacial modes precisely. To obtain the dispersion curve, we then use a medium convergence angle (Fig. 1b) to achieve the best balance between spatial and momentum resolutions. A reasonable momentum resolution (approximately one-quarter of the BZ lateral size) can be achieved when the spatial resolution is bounded by the diffraction limit but is still below 1.5 nm (Extended Data Fig. 1). With a slot aperture, the dispersion diagram can be recorded in parallel, yielding a 4D EELS ($x$–$y$–$\omega$–$q$, where $q$ is the momentum transfer) dataset[21]. Figure 1c, d shows integrated differential phase contrast (iDPC)-STEM images of an atomically abrupt cBN/diamond interface viewed from two representative zone axes, and Fig. 1e, f are corresponding projections of the atomic model.

## Local phonon spectra near the interface

Figure 2a shows the phonon dispersion curves of bulk cBN and diamond calculated by density functional perturbation theory (DFPT). Owing to similar crystal structures, their phonon dispersions are similar, except for the transverse optical (TO) branch. As a polar material, cBN has a finite longitudinal optical (LO)–TO splitting gap, which is absent in diamond. Thus, the DOS peak of the cBN TO phonon is lower than that of diamond, whereas their acoustic DOS peaks have a large overlap. Now we focus on the interface between them. It is well known that surface phonon modes lying below bulk bands appear at crystal surfaces[1,33,34]. At interfaces, however, phonon modes are more complicated and related theories have yet to mature. Recent theoretical studies have classified modes near interfaces into four categories according to their vibration distribution[7,12]: extended modes that involve vibrations on both sides, partially extended modes that vibrate predominately on one side, interfacial modes that are localized at the interface, and isolated modes that are isolated from the interface. The first two types originate from the bulk modes of two materials, which can hybridize to form extended modes if they are degenerate, or form partially extended modes when no degenerate mode exists on the opposite side. The last two types are new features associated with the broken symmetry, with enhanced or reduced vibration at the interface. To verify these predictions, we acquired 3D EELS datasets in an interface region with no nearby defects observed. Figure 2b shows an EELS line profile across the interface. The phonon signal changes abruptly near the interface within approximately 1 nm. Notably, the spectrum near the interface is not simply a linear combination of two bulk spectra. Even if we perform a least-squares fitting to find the

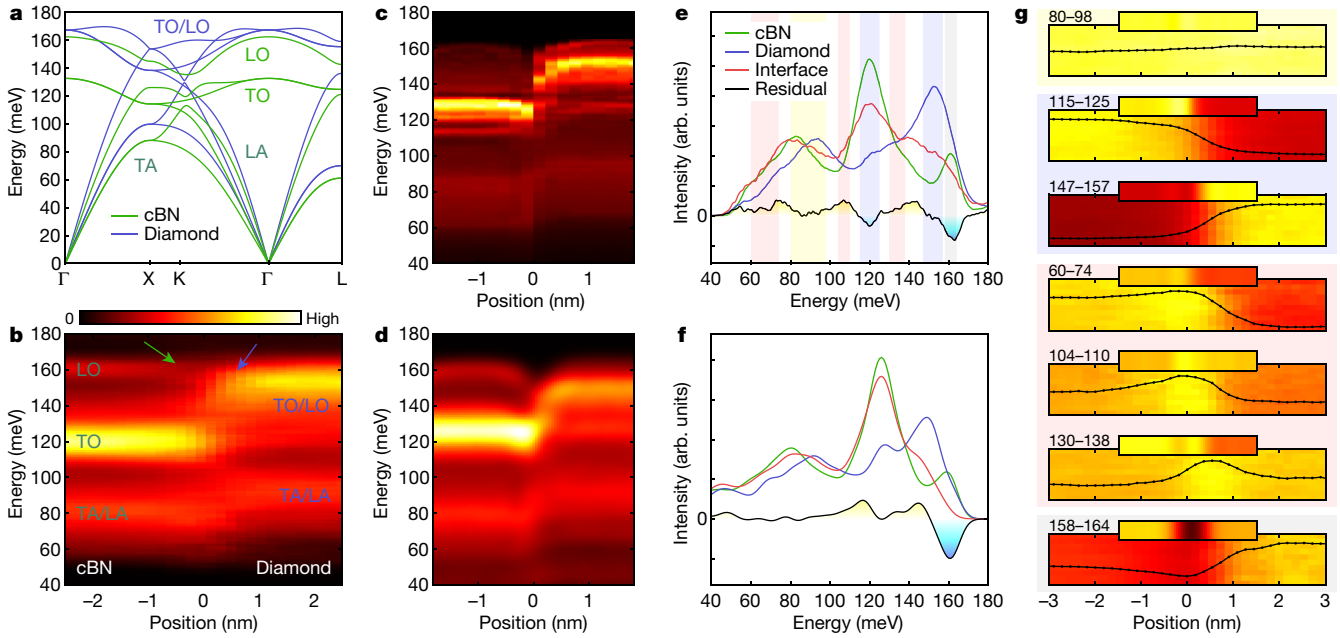


**Fig. 2 | Interface phonon measurements at the atomic scale. a**, The calculated phonon dispersions for bulk cBN (green) and diamond (blue). L(T) stands for longitudinal (transverse) and O(A) stands for optical (acoustic). **b**, The measured EELS line profile across the interface with the beam travelling along the [11$\bar{2}$] direction. The origin of the horizontal axis is at the interface. The green and blue arrows are guides to the eye that mark the intensity decrease of cBN LO phonon and the energy shift of the diamond optical phonon, respectively. **c**, The calculated phonon DOS projected onto atom layers. **d**, The calculated EELS scattering cross-section. **e**, The EEL spectra acquired in cBN (green), in diamond (blue) and at the interface (red). The black curve with gradient filling (where yellow and blue colours represent positive and negative residuals respectively) is the interface component that cannot be expressed as a linear combination of two bulk spectra. Shaded regions indicate the energy integration windows for **g**. **f**, The corresponding calculation results. **g**, Energy-filtered EELS maps. Overlaid lines are averaged intensity profiles, the contrast of which has been adjusted for better visibility. The small inset bars at the top of each map are the calculated maps. The energy integration windows are indicated by numbers (in meV) in the top-left corner of each map, and are also shaded in **e**. In all the colour maps, the lower colour limit is fixed to zero.

linear combination that matches the acquired spectra best, near the interface there is still a large residual that originates from new modes at the interface (Extended Data Fig. 2). For the cBN side, the LO phonon significantly reduces its intensity upon approaching the interface (green arrow); the TO mode and acoustic modes show fewer new features, with only a tiny redshift near the interface. For the diamond side, the TO/LO peak has a large redshift at the interface (blue arrow), whereas the acoustic peak is featureless. Additional measurements in different interface regions give highly reproducible results (Extended Data Fig. 3).

To understand and corroborate these results, we performed DFPT phonon calculations for the interface (Methods). The calculated projected DOS (PDOS) of each atom layer is shown in Fig. 2c. For the carbon layers near the interface, the PDOS is considerably different from that of the bulk diamond. The optical phonon peak is about 10 meV lower than bulk diamond, and this effect is localized within around three carbon layers. For the cBN layers near the interface, qualitatively similar but less prominent redshift behaviour is also observed for the TO peak, and the LO peak almost vanishes at the interface. The calculated EELS line profile (Methods) is shown in Fig. 2d, which agrees nicely with the experiment and successfully reproduces the redshift of the diamond optical phonon and the intensity decrease of the cBN LO phonon. Figure 2e, f compares measured and calculated spectra with the beam located in cBN (green), in diamond (blue) and at the interface (red). The interface component that cannot be obtained from bulk spectra, as extracted by the aforementioned fitting residual, is plotted as the black curves. This residual represents the DOS of the interface phonon modes excluding bulk contributions, with peaks and dips corresponding to interfacial and isolated modes, respectively. By comparing the intensity among spectra acquired in different positions, all four types of modes can be recognized in some energy regions.

For the overlapping region of two bulk acoustic DOS peaks, no remarkable new features were observed at the interface, so the intensity map (first panel in Fig. 2g) is homogenous just as the interface is transparent. This corresponds to extended modes delocalized in the entire system. The optical DOS peaks of the two materials have little overlap, so the intensity maps for the corresponding energy windows (second and third panels in Fig. 2g) show an abrupt intensity change at the interface, characteristic for partially extended modes. Interestingly, we identified three energy windows in which the interface spectrum is higher than both sides, revealing interfacial modes. In the fourth to sixth panels in Fig. 2g, the vibration signal shows a substantial enhancement at the interface. From these three maps, the root-mean-square width of the enhancement is found to be 1.4 nm, 1.0 nm and 0.8 nm, respectively. The first mode (60–74 meV) is less localized mainly owing to the existence of degenerate bulk modes, forming an interface resonance mode as a mixture of the localized mode and the bulk continuum. For the other two modes, the bulk DOS at the same energy is small, so their localization is within 1 nm. By collecting scattered electrons at high-order BZs (off-axis geometry[28,30], Extended Data Fig. 4), one of them can be visualized with a higher contrast, but the main spectrum features are consistent. In addition, at around 160 meV, the interface spectrum is considerably weaker than both sides (bottom panel in Fig. 2g). This is an isolated mode that has significantly reduced vibration at the interface. These observations provide direct experimental evidence of interfacial modes, and also unequivocally reveal the existence of isolated modes that have not yet drawn much attention.

## Dispersion relation measurement

Thus far we have measured local phonon spectra at the atomic scale, but the collected signal is averaged over the whole BZ. However, thermal

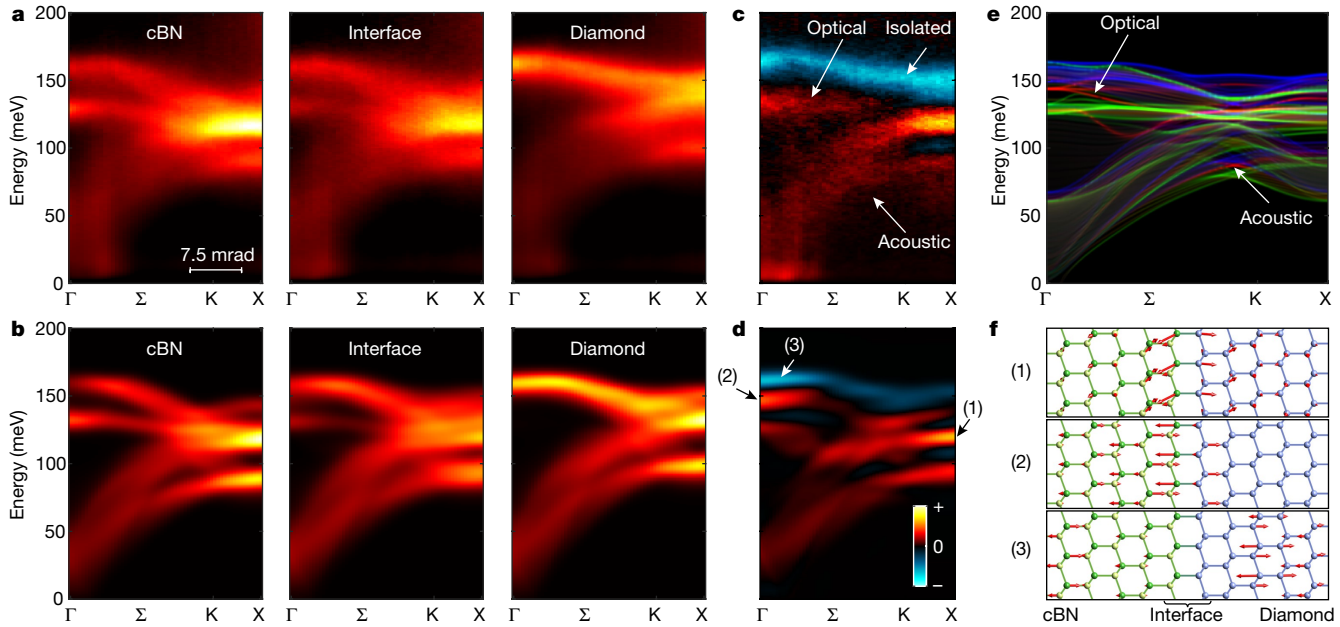


**Fig. 3 | Phonon dispersion measurements at the interface. a**, The measured phonon dispersion diagrams along the Γ–Σ–K–X line with the beam located in cBN (left), at the interface (middle) and in diamond (right). **b**, The corresponding simulation results based on DFPT calculations. **c**, **d**, The measured (**c**) and calculated (**d**) difference between the interface spectra and the average of two bulk spectra. **e**, The calculated phonon dispersion of the interface model, projected onto the (111) interface. Three RGB channels represent the squared norm of the vibration eigenvector of the interface layers (red), cBN (green) and diamond (blue). **f**, Phonon eigenvectors for three typical modes (with their momentum and energy labelled in **d**). The red arrows are the real part of eigenvectors showing the vibration amplitudes of each atom.

conductance, electron–phonon interaction and many other properties depend not only on the DOS but also on the group velocity or dispersion relation that cannot be obtained without momentum resolution[2]. We next employ the 4D EELS technique to measure the phonon dispersion of the interfacial modes. At the interface, the phonon dispersion can only be defined in a two-dimensional interface BZ (a slice of the bulk BZ parallel to the interface plane) due to the broken translational symmetry along [111] (Extended Data Fig. 5). The slot aperture was placed along Γ–Σ–K–X line, the common high-symmetry line of the bulk BZ and the interface BZ (inset in Fig. 1a). Although the dispersion can be measured nicely with smaller convergence angles (Extended Data Fig. 5), the required nanometre spatial resolution leads to a better balance at a medium angle (Methods). Figure 3a shows the measured dispersion with the beam located in cBN, at the interface and in diamond, and Fig. 3b is the corresponding DFPT calculation results. For completeness, Supplementary Video 1 illustrates the acquired dispersion diagram as a function of the beam position. EELS line profiles at five momentum transfers are given in Extended Data Fig. 6, where spectral features of interfacial modes and isolated modes are directly visible. Although subtle, new features at the interface can be recognized by subtracting the averaged bulk spectra from the interface spectra, as shown in Fig. 3c, d. The experimental diagram in Fig. 3c is sensitive to noise after this subtraction, but decent agreement with the calculation is still achieved owing to our high detection sensitivity. Interfacial localized modes appear below 150 meV, where both acoustic and optical branches are recognizable. The acoustic branch has increasing energy from the BZ centre to the BZ boundary, which may aid thermal transport laterally along the interface owing to their large group velocity, whereas the optical branch is mostly dispersionless. In addition, there is a dispersion line with negative intensity at 150–160 meV, which corresponds to an isolated mode. The measured dispersion here can be validated not only by the calculation but also by its consistency with results shown in Fig. 2. The flat interfacial optical band gives rise to an enhanced phonon PDOS at approximately 140 meV, and the negative signal here sums up to a decreased signal at approximately 160 meV.

To better interpret these spectra, the calculated phonon dispersion of the interface model projected onto the (111) interface is shown in Fig. 3e, where three colour channels are used to represent vibration amplitudes at the interface (red), in cBN (green) and in diamond (blue). The green and blue regions originate from projected bulk phonon bands (Extended Data Fig. 7). In addition, we observe new dispersion lines (reddish lines) localized at the interface. For the three representative modes marked by arrows in Fig. 3d, Fig. 3f shows their calculated phonon eigenvectors. Both interfacial acoustic and optical modes (top and middle panels) have a large vibration amplitude at the interface, decaying to nearly zero within a few atom layers; the isolated mode (bottom panel) has considerable vibration amplitudes in both materials away from the interface, but has a vanishing amplitude at the interface. Thus, the measured positive signal in Fig. 3c directly reveals the dispersion relation of interfacial modes, and the negative line gives the dispersion relation of isolated modes.

## Discussion and outlook

The new vibrational modes measured here are expected to substantially affect thermal transport across the interface. The traditional phonon gas model[35,36] and the atomistic Green's function method[37] describe the ITC by the transmittance of bulk phonon modes without considering detailed vibrational modes near the interface. However, such an extensively used simplification is challenged by recent molecular dynamics simulations[7,12]. To see how interfacial modes contribute to thermal transport, we performed the interface conductance modal analysis[38], with the results shown in Extended Data Fig. 8 (Methods). Interfacial modes around 140 meV show strong correlations with almost all other modes, indicating that they scatter frequently with bulk modes on both sides and thus serve as an intermediate state of energy transfer. In contrast, isolated modes hardly correlate with any mode and give almost no contribution to the ITC. They have reduced amplitudes at the interface and separate bulk modes in space, making energy exchange between two materials much harder. Therefore, direct measurement

of interfacial and isolated modes can provide useful information for the thermal transport properties for a given interface.

Interfacial modes can also be important in electron transport owing to electron–phonon coupling. Two-dimensional electron gases can form at interfaces and are especially useful in transistor-like semiconductor structures[39]. As an example, a two-dimensional electron gas is predicted to form at the cBN/diamond interface[40], which has an orders-of-magnitude stronger electron–phonon coupling with interfacial phonon modes than with bulk modes (Extended Data Fig. 9). In addition, the interface between two topologically inequivalent phononic materials can also be of particular interest, where topological interface phonon modes are predicted to form[41–43]. Direct experimental verification of this also requires nanoscale dispersion measurements.

In summary, we have demonstrated a 4D EELS measurement of interface phonon dispersion, revealing vibrational properties at a heterointerface including interfacial modes and isolated modes. This information should be useful for a variety of topics in physics, materials science and chemistry, such as thermal conductance, electron transport and topological phononics. The demonstrated ability to measure interface phonon dispersion should also stimulate practical research towards thermal engineering of interfaces and related technologies.

## Online content

Any methods, additional references, Nature Research reporting summaries, source data, extended data, supplementary information, acknowledgements, peer review information; details of author contributions and competing interests; and statements of data and code availability are available at https://doi.org/10.1038/s41586-021-03971-9.


1. Masri, P. Surface and interface phonons and related topics. *Surf. Sci. Rep.* **9**, 293–369 (1988).
2. Giri, A. & Hopkins, P. E. A review of experimental and computational advances in thermal boundary conductance and nanoscale thermal transport across solid interfaces. *Adv. Funct. Mater.* **30**, 1903857 (2020).
3. Djafari-Rouhani, B., Masri, P. & Dobrzynski, L. Vibrational properties of a bicrystal interface: different-interface phonons and the low-temperature specific heat. *Phys. Rev. B* **15**, 5690–5711 (1977).
4. Masri, P. Interface phonons: effects of crystal size. *J. Phys. C* **14**, 2265–2278 (1981).
5. Tamine, M., Boumrar, H. & Rafil, O. Interface and step localized phonon modes between two truncated thin films. *Surf. Rev. Lett.* **11**, 155–165 (2004).
6. Girvin, S. & Yang, K. *Modern Condensed Matter Physics* (Cambridge Univ. Press, 2019).
7. Gordiz, K. & Henry, A. Phonon transport at interfaces: determining the correct modes of vibration. *J. Appl. Phys.* **119**, 015101 (2016).
8. Luh, D. A., Miller, T., Paggel, J. J. & Chiang, T. C. Large electron–phonon coupling at an interface. *Phys. Rev. Lett.* **88**, 256802 (2002).
9. Cahill, D. G. et al. Nanoscale thermal transport. *J. Appl. Phys.* **93**, 793–818 (2003).
10. Chu, C. W. et al. Interface-induced and interface-enhanced superconductivity. *J. Supercond. Nov. Magn.* **32**, 7–15 (2018).
11. Wang, Q.-Y. et al. Interface-induced high-temperature superconductivity in single unit-cell FeSe films on $SrTiO_3$. *Chin. Phys. Lett.* **29**, 037402 (2012).
12. Gordiz, K. & Henry, A. Phonon transport at crystalline Si/Ge interfaces: the role of interfacial modes of vibration. *Sci. Rep.* **6**, 23139 (2016).
13. Burkel, E. Phonon spectroscopy by inelastic X-ray scattering. *Rep. Prog. Phys.* **63**, 171–232 (2000).
14. Lee, J., Crampton, K. T., Tallarida, N. & Apkarian, V. A. Visualizing vibrational normal modes of a single molecule with atomically confined light. *Nature* **568**, 78–82 (2019).
15. Chen, X. et al. Modern scattering-type scanning near-field optical microscopy for advanced material research. *Adv. Mater.* **31**, 1804774 (2019).
16. Szeftel, J. Surface phonon dispersion, using electron energy loss spectroscopy. *Surf. Sci.* **152/153**, 797–810 (1985).
17. Krivanek, O. L. et al. Vibrational spectroscopy in the electron microscope. *Nature* **514**, 209–212 (2014).
18. Egerton, R. F. *Electron Energy-loss Spectroscopy in the Electron Microscope* 3rd edn (Springer, 2011).
19. Hage, F. S. et al. Nanoscale momentum-resolved vibrational spectroscopy. *Sci. Adv.* **4**, eaar7495 (2018).
20. Lagos, M. J., Trugler, A., Hohenester, U. & Batson, P. E. Mapping vibrational surface and bulk modes in a single nanocube. *Nature* **543**, 529–532 (2017).
21. Qi, R. et al. Four-dimensional vibrational spectroscopy for nanoscale mapping of phonon dispersion in BN nanotubes. *Nat. Commun.* **12**, 1179 (2021).
22. Li, N. et al. Direct observation of highly confined phonon polaritons in suspended monolayer hexagonal boron nitride. *Nat. Mater.* **20**, 43–48 (2021).
23. Govyadinov, A. A. et al. Probing low-energy hyperbolic polaritons in van der Waals crystals with an electron microscope. *Nat. Commun.* **8**, 95 (2017).
24. Venkatraman, K., Levin, B. D. A., March, K., Rez, P. & Crozier, P. A. Vibrational spectroscopy at atomic resolution with electron impact scattering. *Nat. Phys.* **15**, 1237–1241 (2019).
25. Hage, F. S., Radtke, G., Kepaptsoglou, D. M., Lazzeri, M. & Ramasse, Q. M. Single-atom vibrational spectroscopy in the scanning transmission electron microscope. *Science* **367**, 1124–1127 (2020).
26. Yan, X. et al. Single-defect phonons imaged by electron microscopy. *Nature* **589**, 65–69 (2021).
27. Senga, R. et al. Position and momentum mapping of vibrations in graphene nanostructures. *Nature* **573**, 247–250 (2019).
28. Dwyer, C. et al. Electron-beam mapping of vibrational modes with nanometer spatial resolution. *Phys. Rev. Lett.* **117**, 256101 (2016).
29. Hachtel, J. A. et al. Identification of site-specific isotopic labels by vibrational spectroscopy in the electron microscope. *Science* **363**, 525–528 (2019).
30. Hage, F. S., Kepaptsoglou, D. M., Ramasse, Q. M. & Allen, L. J. Phonon spectroscopy at atomic resolution. *Phys. Rev. Lett.* **122**, 016103 (2019).
31. Plotkin-Swing, B. et al. Hybrid pixel direct detector for electron energy loss spectroscopy. *Ultramicroscopy* **217**, 113067 (2020).
32. Nicholls, R. J. et al. Theory of momentum-resolved phonon spectroscopy in the electron microscope. *Phys. Rev. B* **99**, 094105 (2019).
33. Fritsch, J., Pavone, P. & Schröder, U. Ab initio calculation of the phonon dispersion in bulk InP and in the InP(110) surface. *Phys. Rev. B* **52**, 11326–11334 (1995).
34. Benedek, G. et al. Theory of surface phonons at metal surfaces: recent advances. *J. Phys. Condens. Matter* **22**, 084020 (2010).
35. Little, W. A. The transport of heat between dissimilar solids at low temperatures. *Can. J. Phys.* **37**, 334–349 (1959).
36. Swartz, E. T. & Pohl, R. O. Thermal boundary resistance. *Rev. Mod. Phys.* **61**, 605–668 (1989).
37. Mingo, N. & Yang, L. Phonon transport in nanowires coated with an amorphous material: an atomistic Green's function approach. *Phys. Rev. B* **68**, 245406 (2003).
38. Gordiz, K. & Henry, A. A formalism for calculating the modal contributions to thermal interface conductance. *New J. Phys.* **17**, 103002 (2015).
39. Ohtomo, A. & Hwang, H. Y. A high-mobility electron gas at the $LaAlO_3/SrTiO_3$ heterointerface. *Nature* **427**, 423–426 (2004).
40. Chen, C. et al. Misfit accommodation mechanism at the heterointerface between diamond and cubic boron nitride. *Nat. Commun.* **6**, 6327 (2015).
41. Süsstrunk, R. & Huber, S. D. Observation of phononic helical edge states in a mechanical topological insulator. *Science* **349**, 47–50 (2015).
42. Li, J. et al. Computation and data driven discovery of topological phononic materials. *Nat. Commun.* **12**, 1204 (2021).
43. Liu, Y., Xu, Y., Zhang, S.-C. & Duan, W. Model for topological phononics and phonon diode. *Phys. Rev. B* **96**, 064106 (2017).

# Methods

### Sample preparation

In this study, we chose the epitaxial cBN/diamond heterojunction[44]—the heterojunction between top two thermal-conducting materials[45,46]—as a model system. First-principles calculations predicted an extremely high ITC for their heterojunction[47], making them promising for thermal management in high-power devices. The cBN crystals were grown epitaxially on the diamond substrates by the temperature gradient method under high-temperature and high-pressure conditions[44]. TEM samples were prepared by the focused ion beam (FIB) technique (Hitachi FB2200 FIB) with a gallium ion source. To clean the damaged layer of the TEM samples induced by the ion radiation of FIB, argon ion-milling with an accelerating voltage of 0.5 kV was performed using a precision ion polishing system (Model 691, Gatan). The film thickness in our region of interest is 50–60 nm. The lattice mismatch between cBN and diamond is only 1.4% and the strain is released by a periodic stacking fault network[40]. In the region between two neighbouring stack faults, the interface is coherent and atomically flat, providing a clean platform for our study. At the interface, cBN is terminated with boron atoms that are directly bonded to carbon atoms on the diamond side[40]. The same sample has also been carefully characterized elsewhere[40], confirming the atomic abruptness of the interface.

### EELS data acquisition

The EELS data were acquired on a Nion U-HERMES200 microscope equipped with both a monochromator and aberration correctors. Three-dimensional EELS datasets were acquired with 60-kV beam energy, 35-mrad convergence semi-angle and 25-mrad collection semi-angle. For off-axis datasets, the central diffraction spot was fully displaced away from the EELS aperture[30]; for other datasets, no such displacement was applied. The typical dwell time was 400–800 ms per pixel and approximately 30 min for each dataset in total. The sample drift was usually within 1 nm on this timescale and was corrected afterwards by aligning the interface. The typical energy resolution under these conditions was 10–12 meV. The typical spatial resolution was 0.2 nm.

Four-dimensional EELS datasets were acquired with 30-kV beam energy and 7.5-mrad convergence semi-angle. A slot aperture with aspect ratio 16:1 was placed along the Γ–Σ–K–X line. The use of the slot aperture enables parallel acquisition among different momentum transfers. Compared with the serial acquisition method[19,27], it greatly enhances data acquisition efficiency and gives a better momentum resolution along the aperture when the convergence angle is the same[21]. It also makes the signal intensity among different momentum transfers consistent and makes it easy for them to be compared. To avoid the strong central diffraction spot and enhance the signal-to-background ratio, the slot aperture was displaced along Γ–L direction by a reciprocal lattice vector (Extended Data Fig. 6a). The typical dwell time was 15–20 s per pixel and approximately 40 min for each dataset in total. The typical energy resolution was 10–12 meV. The typical spatial resolution was 1.3 ± 0.2 nm.

### EELS data processing

All acquired spectra were processed by custom-written MATLAB (R2019b) code. For each dataset, EEL spectra were first registered by their normalized cross-correlation to correct beam energy drifts. A block-matching and 3D filtering algorithm was then applied to remove Gaussian noise[48,49]. The data were individually denoised in two spatial dimensions for each energy and momentum channel, where the noise level was estimated based on high-frequency elements in the Fourier domain.

For 3D EELS datasets, the spectra were normalized by the zero-loss peak (ZLP) total intensity. The ZLP was removed by fitting the spectra to a Pearson function in two energy windows, one before and one after the energy loss region (approximately 20–45 meV and 180–220 meV, but slightly adjusted for each dataset to achieve the best fitting). Lucy–Richardson deconvolution was then employed to ameliorate the broadening effect caused by the finite energy resolution, taking the ZLP as the point spread function.

For 4D EELS datasets, a correction for the statistical factor was performed following literature[50]. This process suppresses low-energy peaks because they have a higher occupation number. After the correction, the ZLP is automatically vanishingly small and can be neglected.

### Spatial resolution estimation

In our settings, there are three main factors that affect the beam size: the diffraction limit, the beam source size and spherical aberrations[26,51]. The first two terms are inversely proportional to the convergence semi-angle $\alpha$, so when $\alpha$ is small, the aberration term can be ignored (as verified by our results below). The diffraction limit as a function of $\alpha$ is plotted as solid lines in Extended Data Fig. 1a, b, and the dashed lines are the calculated beam size considering both terms. To experimentally estimate the resolution, we quantitatively compare high-angle annular dark field (HAADF) images of gold nanoparticles taken with different $\alpha$ (Extended Data Fig. 1d–k)[21]. First, a reference image was taken with a sufficiently large $\alpha$, where atomic resolution can be achieved. Multiple images were then taken with various smaller $\alpha$ in the same sample region. The reference image was convoluted with a Gaussian kernel, the width of which was determined by least-squares fitting the convoluted image to the image acquired with small $\alpha$. The fitted full-width at half-maximum (FWHM) of the Gaussian kernel represents the spatial resolution in real experiments. We found our experimental beam size is readily very close to the diffraction-limited theoretical lower bound (Extended Data Fig. 1a, b). The beam size in our 4D EELS setting (7.5 mrad at 30 kV) was fitted to be 1.3 ± 0.2 nm, which is only about 15% larger than the ultimate diffraction limit.

### Ab initio calculations

Density functional theory calculations were performed using Quantum ESPRESSO[52,53] with the Perdew–Zunger exchange-correlation functional[54] and the Vanderbilt ultrasoft pseudopotential[55]. The kinetic energy cut-off was 80 Rydbergs (Ry) for wavefunctions and 800 Ry for charge density and potential. The interface model contains 12 layers of carbon atoms connected to 12 layers of cBN (48 atoms in one hexagonal unit cell with cell parameters $a$ = 2.518 Å and $c$ = 49.301 Å). The small lattice mismatch between cBN and diamond was ignored. The structure was optimized under the $C_{3v}$ group symmetry constraint until the residual force was below $10^{-4}$ Ry per Bohr on every atom. The dynamical matrices and force constants were obtained using DFPT. The phonon dispersion and PDOS was calculated by interpolating the dynamical matrix on a 6 × 6 × 1 $q$-mesh. Compared with a smaller model with 36 atoms in one unit cell, no noticeable change in phonon PDOS was observed, indicating that our model is large enough to exclude couplings between interfaces owing to periodic boundary conditions. The calculated phonon dispersion contains tiny imaginary frequencies owing to common numerical instabilities, but the imaginary frequencies only appear in a small region around the Γ point occupying 0.003% of the total phonon DOS and can be safely neglected. Electron–phonon coupling calculation for the interface model was performed with a 48 × 48 × 4 dense mesh of $k$-points for the sum of electron–phonon coefficients at the Fermi energy, as implemented in Quantum ESPRESSO.

### Scattering cross-section

For an infinite bulk crystal, the wavefunction of the electron beam can be treated as plane waves and then the differential scattering cross-section $\mathrm{d}^2\sigma/\mathrm{d}\omega\mathrm{d}\Omega$ can be calculated as[20,27,32]

$$\frac{\mathrm{d}^2\sigma}{\mathrm{d}\omega\mathrm{d}\Omega} \propto \sum_{\text{mode }\lambda} |F_\lambda(\mathbf{q})|^2 \left[ \frac{n+1}{\omega_\lambda(\mathbf{q})}\delta(\omega-\omega_\lambda(\mathbf{q})) + \frac{n}{\omega_\lambda(\mathbf{q})}\delta(\omega+\omega_\lambda(\mathbf{q})) \right] \quad (1)$$

where $\omega_\lambda(\mathbf{q})$ and $n$ are the frequency and occupancy number of the $\lambda$th phonon mode with wavevector $\mathbf{q}$. $\delta(x)$ is the Dirac delta function. The coupling factor

$$F_\lambda(\mathbf{q}) \propto \frac{1}{q^2} \sum_{\text{atom } k} \frac{1}{\sqrt{M_k}} e^{-i\mathbf{q}\cdot\mathbf{r}_k} e^{-W_k(\mathbf{q})} Z_k(\mathbf{q}) [\mathbf{e}_\lambda(k, \mathbf{q}) \cdot \mathbf{q}] \quad (2)$$

is determined by the mass $M_k$, real-space position $\mathbf{r}_k$, effective charge $Z_k(\mathbf{q})$, Debye–Waller factor[56] $\exp(-2W_k(\mathbf{q}))$ and phonon eigenvector $\mathbf{e}_\lambda(k, \mathbf{q})$ of the $k$th atom in a unit cell. The effective charge $Z_k(\mathbf{q})$ was calculated following literature[32] with atomic form factors constructed from parameters in the literature[57]. When the collection range of the EELS aperture is large enough to include multiple BZs, the summation of the squared coupling factor approximately gives the phonon DOS.

For the interface, approximating the beam as plane waves is no longer valid. We model it as a Gaussian beam instead. Then the position-dependent coupling factor can be approximated as

$$F_\lambda(\mathbf{q}, \mathbf{R}) \propto \frac{1}{q^2} \sum_{\text{atom } k} \frac{1}{\sqrt{M_k}} \mathcal{G}(|\bar{\mathbf{r}}_k - R|) e^{-i\mathbf{q}\cdot\mathbf{r}_k} e^{-W_k(\mathbf{q})} Z_k(\mathbf{q}) [\mathbf{e}_\lambda(k, \mathbf{q}) \cdot \mathbf{q}] \quad (3)$$

where $\mathbf{R} = (X, Y)$ stands for the 2D position of the electron beam, the overbar on $\mathbf{r}_k$ means only taking its first two components and $\mathcal{G}$ is the Gaussian function with its width determined by the spatial resolution. The EEL spectra were simulated by summing in the momentum space in a region corresponding to the EELS aperture, convoluted by the angle distribution of the incident beam.

### Molecular dynamics simulations

The equilibrium molecular dynamics simulations were performed using the LAMMPS package[58] with the Tersoff interatomic potential parametrized in ref. [59]. The modal contribution to the ITC was calculated within the framework of interface conductance modal analysis[12,38,60], which combines the Green–Kubo method for thermal conductance and the modal decomposition of the heat flux. A detailed methodology is given in refs. [7,12,38,60]. In short, the ITC $G$ is defined as the heat flux across the interface per unit temperature drop, which characterizes the ability of the interface to conduct heat between two sides. The ITC and the instantaneous heat flux across the interface $Q(t)$ at time $t$ are related by the Green–Kubo formula

$$G = \frac{1}{Ak_B T^2} \int_0^\infty \langle Q(t)Q(0) \rangle \, dt$$

where $A$ is the interface area, $k_B$ denotes the Boltzmann constant, $T$ is the temperature of the system, and angle brackets denote temporal correlation function averaged with different time origins. The instantaneous heat flux across the interface is defined as

$$Q = -\frac{1}{2} \sum_{i \in \text{cBN}} \sum_{j \in \text{diamond}} \mathbf{f}_{ij} \cdot (\dot{\mathbf{x}}_i + \dot{\mathbf{x}}_j)$$

where $\mathbf{f}_{ij}$ is the interatomic force between atom $i$ and atom $j$, and $\dot{\mathbf{x}}$ is the atomic velocity. Applying modal analysis, the atomic coordinates are transformed into modal coordinates, and hence the heat flux $Q$ can be projected onto modal contributions $Q = \sum_n Q_n$, where $n$ labels the phonon mode. Thus, the ITC can be expressed as a double summation of mode–mode correlation between the $n$th and $n'$th modes

$$G = \sum_n \sum_{n'} G_{nn'} = \sum_n \sum_{n'} \frac{1}{Ak_B T^2} \int_0^\infty \langle Q_n(t) Q_n(0) \rangle dt$$

or, upon summation on $n'$ first, expressed as a single summation of modal heat conductance $G = \sum_n G_n$. In practice, the DFPT-calculated phonon eigenvectors were used as the basis vectors in the modal analysis. The force routine in LAMMPS was modified to calculate and dump $Q_n$. Custom MATLAB code was then used to calculate the correlation function of the modal heat flux. The result was averaged from 50 independent simulations for 2,880 atoms. In each simulation, after an initial structure relaxation under temperature control at 300 K using velocity rescaling, the heat flux was calculated while running the simulation in the microcanonical ensemble for 1 ns with a time step of 1 fs. Extended Data Fig. 8 shows the calculated ITC decomposed into mode–mode correlations $G_{nn'}$ (qualitatively it represents the interaction strength between two modes). The mode correlation map as a function of two phonon frequencies is shown in Extended Data Fig. 8a, in which interfacial modes at approximately 140 meV have strong correlations with almost all other modes. This can be understood in terms of an inelastic phonon scattering process. As the three-phonon scattering matrix element involves the product of three phonon eigenvectors[61], partially extended modes on two sides cannot directly exchange energy inelastically owing to little amplitude overlapping. The interfacial modes, however, have significant amplitude overlapping with modes on both sides, and thus interact strongly with them facilitating inelastic heat transfer. In contrast, isolated modes at approximately 160 meV have little correlation with any mode. The mode correlation map in Extended Data Fig. 8b is plotted as a function of interfacial amplitudes of two phonon modes. It is more evident that modes with higher amplitudes at the interface generally make larger contributions to the ITC.

## Data availability

The experimental 3D EELS and 4D EELS datasets are available in the Open Science Framework repository at https://osf.io/8mp4t. The other data that support the findings of this study are available from the corresponding author upon request.

## Code availability

A GUI version of the MATLAB code for the EELS data processing can be found on GitHub at https://github.com/ruishiqi/EELS.


44. T. Taniguchi, & S. Yamaoka. Heteroepitaxial growth of cubic boron nitride single crystal on diamond seed under high pressure. *Mater. Res. Soc. Symp. Proc.* **472**, 379–383 (1997).
45. Chen, K. et al. Ultrahigh thermal conductivity in isotope-enriched cubic boron nitride. *Science* **367**, 555–559 (2020).
46. Wei, L., Kuo, P. K., Thomas, R. L., Anthony, T. R. & Banholzer, W. F. Thermal conductivity of isotopically modified single crystal diamond. *Phys. Rev. Lett.* **70**, 3764–3767 (1993).
47. Huang, X. & Guo, Z. High thermal conductance across c-BN/diamond interface. *Diam. Relat. Mater.* **108**, 107979 (2020).
48. Zhou, J. et al. Observing crystal nucleation in four dimensions using atomic electron tomography. *Nature* **570**, 500–503 (2019).
49. Dabov, K., Foi, A., Katkovnik, V. & Egiazarian, K. Image denoising by sparse 3-D transform-domain collaborative filtering. *IEEE Trans. Image Process.* **16**, 2080–2095 (2007).
50. Batson, P. E. & Lagos, M. J. Interpretation of meV resolution phonon EELS data. *Microsc. Microanal.* **24**, 412–413 (2018).
51. Williams, D. B. & Carter, C. B. *Transmission Electron Microscopy: A Textbook for Materials Science* Vol. 2 (Springer Science & Business Media, 2008).
52. Giannozzi, P. et al. Quantum ESPRESSO: a modular and open-source software project for quantum simulations of materials. *J. Phys. Condens. Matter* **21**, 395502 (2009).
53. Giannozzi, P. et al. Advanced capabilities for materials modelling with Quantum ESPRESSO. *J. Phys. Condens. Matter* **29**, 465901 (2017).
54. Perdew, J. P. & Zunger, A. Self-interaction correction to density-functional approximations for many-electron systems. *Phys. Rev. B* **23**, 5048–5079 (1981).
55. Vanderbilt, D. Soft self-consistent pseudopotentials in a generalized eigenvalue formalism. *Phys. Rev. B* **41**, 7892–7895 (1990).
56. Vila, F. D., Rehr, J. J., Rossner, H. H. & Krappe, H. J. Theoretical X-ray absorption Debye–Waller factors. *Phys. Rev. B* **76**, 014301 (2007).
57. Waasmaier, D. & Kirfel, A. New analytical scattering-factor functions for free atoms and ions. *Acta Crystallogr. A* **51**, 416–431 (1995).
58. Plimpton, S. Fast parallel algorithms for short-range molecular dynamics. *J. Comput. Phys.* **117**, 1–19 (1995).
59. Kınacı, A., Haskins, J. B., Sevik, C. & Çağın, T. Thermal conductivity of BN-C nanostructures. *Phys. Rev. B* **86**, 115410 (2012).
60. Seyf, H. R., Gordiz, K., DeAngelis, F. & Henry, A. Using Green–Kubo modal analysis (GKMA) and interface conductance modal analysis (ICMA) to study phonon transport with molecular dynamics. *J. Appl. Phys.* **125**, 081101 (2019).
61. Togo, A., Chaput, L. & Tanaka, I. Distributions of phonon lifetimes in Brillouin zones. *Phys. Rev. B* **91**, 094306 (2015).

**Acknowledgements** This work was supported by the National Key R&D Program of China (2019YFA0708200), the National Natural Science Foundation of China (11974023, 52021006, 52125307, 12004010, 11888101), the Key-Area Research and Development Program of Guangdong Province (2018B030327001, 2018B010109009), the Strategic Priority Research Program of Chinese Academy of Sciences (XDB33000000), the '2011 Program' from the Peking-Tsinghua-IOP Collaborative Innovation Center of Quantum Matter, the Youth Innovation Promotion Association of CAS, and the Introduced Innovative R&D Team Project of 'The Pearl River Talent Recruitment Program' of Guangdong Province (2019ZT08C321). We acknowledge the Electron Microscopy Laboratory of Peking University for the use of electron microscopes. We acknowledge the High-performance Computing Platform of Peking University for providing computational resources for the DFPT and molecular dynamics calculations. We thank J. Feng, Q. Gu, A. Gabourie, Z. Fan, C. Shi and T. Lovejoy for helpful discussions; and T. Taniguchi at NIMS in Japan for providing the samples.

**Author contributions** R.Q. and R.S. contributed equally to this work (order determined by a random process upon completion of the manuscript). P.G., R.S. and R.Q. conceived the project. C.C. prepared the TEM sample. R.S. designed and performed the EELS measurements. R.Q. wrote the data processing codes and analysed the data. R.S. and R.Q. performed DFPT calculations of phonon dispersion, scattering cross-section and electron–phonon coupling under the direction of E.-G.W. R.Q., Y.L. and R.S. performed molecular dynamics simulations with the guidance from J.C. Y.S., M.W. and Y.L. acquired atomic-resolution iDPC images. N.L., J.D., K.L., F.W. and D.Y helped the data interpretation. R.Q., R.S. and P.G. finalized the manuscript with inputs from F.W. All authors contributed to this work through useful discussion and/or comments to the manuscript. P.G. supervised the project.

**Competing interests** The authors declare no competing interests.

**Additional information**

**Supplementary information** The online version contains supplementary material available at https://doi.org/10.1038/s41586-021-03971-9.

**Correspondence and requests for materials** should be addressed to Peng Gao.

**Peer review information** *Nature* thanks Juan-Carlos Idrobo, Lucas Lindsay and the other, anonymous, reviewer(s) for their contribution to the peer review of this work. Peer reviewer reports are available.

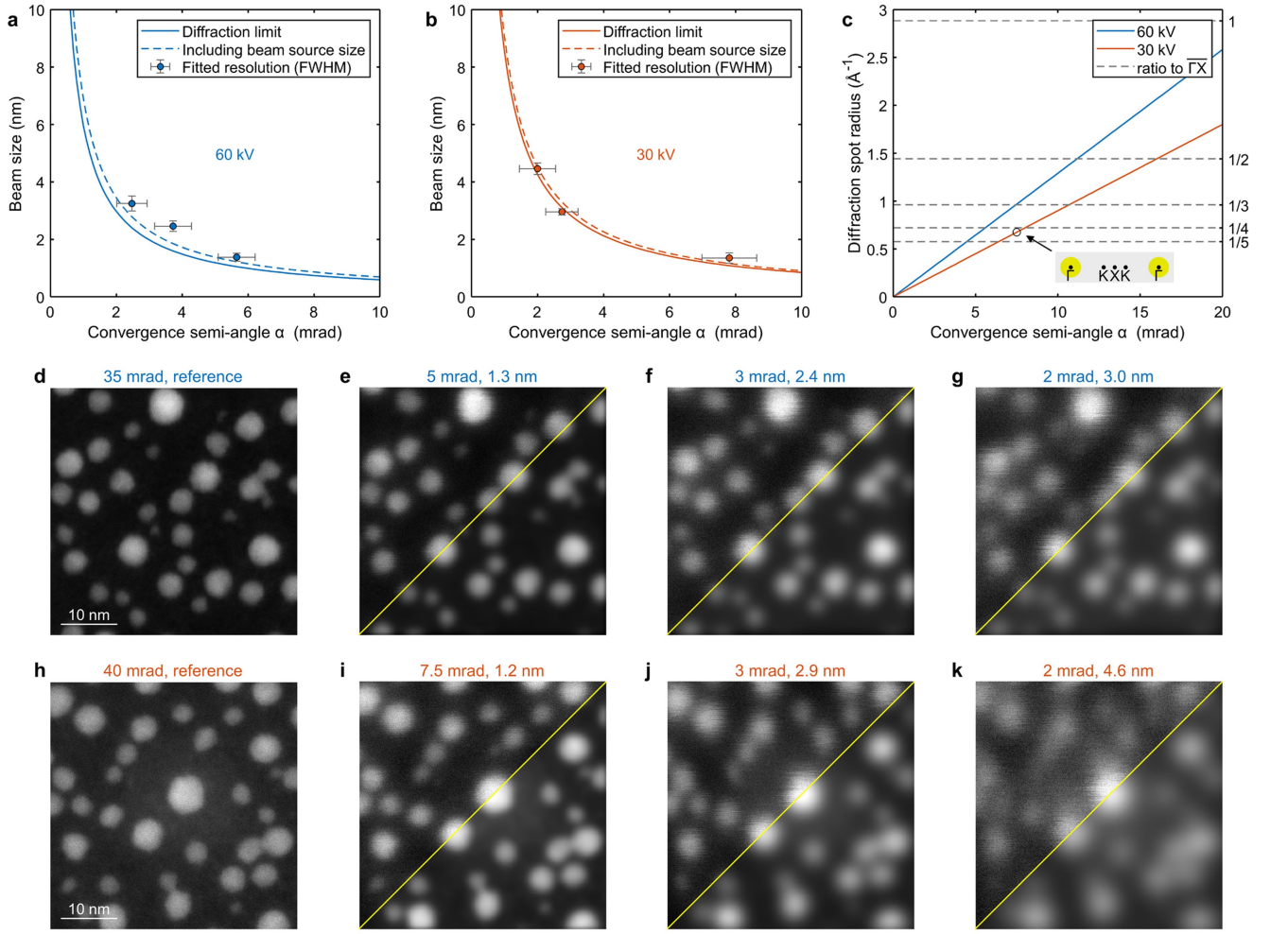


**Extended Data Fig. 1 | Spatial resolution estimation for 4D EELS. a**, **b**, Spatial resolution as a function of convergence semi-angle for 60 kV (**a**) and 30 kV (**b**) beam energy. Solid line, diffraction limit. Dashed line, theoretical beam size considering both the diffraction limit and the beam source size. Scatters with error bars are experimental fitted resolution as shown in the following panels, where vertical error bars represent the standard deviation of the fitted resolutions from multiple images and horizontal ones are estimated by the roundness of the central diffraction spot. See Methods for detail. **c**, Momentum resolution as a function of convergence semi-angle. Inset with light-grey shadow schematically shows the diffraction spot size (yellow circles) relative to the BZ size in our 4D EELS measurements. Dashed horizontal lines mark the ratio to the distance between Γ and X. **d**, HAADF image of gold nanoparticles taken with 35 mrad (nominal value) convergence semi-angle with 60 kV beam energy, serving as a reference image. **e**–**g**, Above the yellow line are typical HAADF images taken with 5 mrad, 3 mrad and 2 mrad convergence semi-angles, respectively. Below the yellow line are the reference image convoluted with a Gaussian kernel with FWHM indicated in the title (fitting result), which agrees nicely with the acquired images above the yellow line. **h**–**k**, same as **d**–**g**, but taken with 30 kV beam energy. Convergence semi-angles are 40 mrad (reference image), 7.5 mrad, 3 mrad, and 2 mrad respectively.

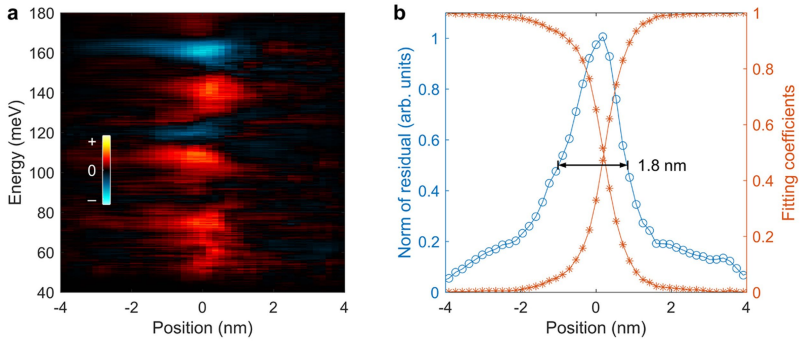


**Extended Data Fig. 2 | Interface component of the spectra extracted by finding the minimum difference between the measured spectrum and all possible linear combinations of two bulk spectra.** The fitting was performed by minimizing $||S(\omega) - a_1 S_{\mathrm{cBN}}(\omega) - a_2 S_{\mathrm{diamond}}(\omega)||$, where $S(\omega)$ is the measured spectrum (Fig. 2b), $S(\omega)$ with subscripts means the bulk spectra, and $a_1$, $a_2$ are adjusted coefficients. **a**, Line profile of the fitting residual. Since the fitting gives the linear combination that is closest to the measured spectrum, the residual represents the interface component that cannot be obtained from bulk modes. Near the interface, three red peaks correspond to three interfacial modes in Fig. 2g. The blue region at 160 meV is due to the isolated mode with reduced vibration at the interface. **b**, Norm (root sum squared) of residuals as a function of position (left axis), and the fitting coefficients $a_1$ and $a_2$ (right axis). The residual is sharply peaked at the interface (FWHM = 1.8 nm), indicating new vibrational features are highly localized at the interface.

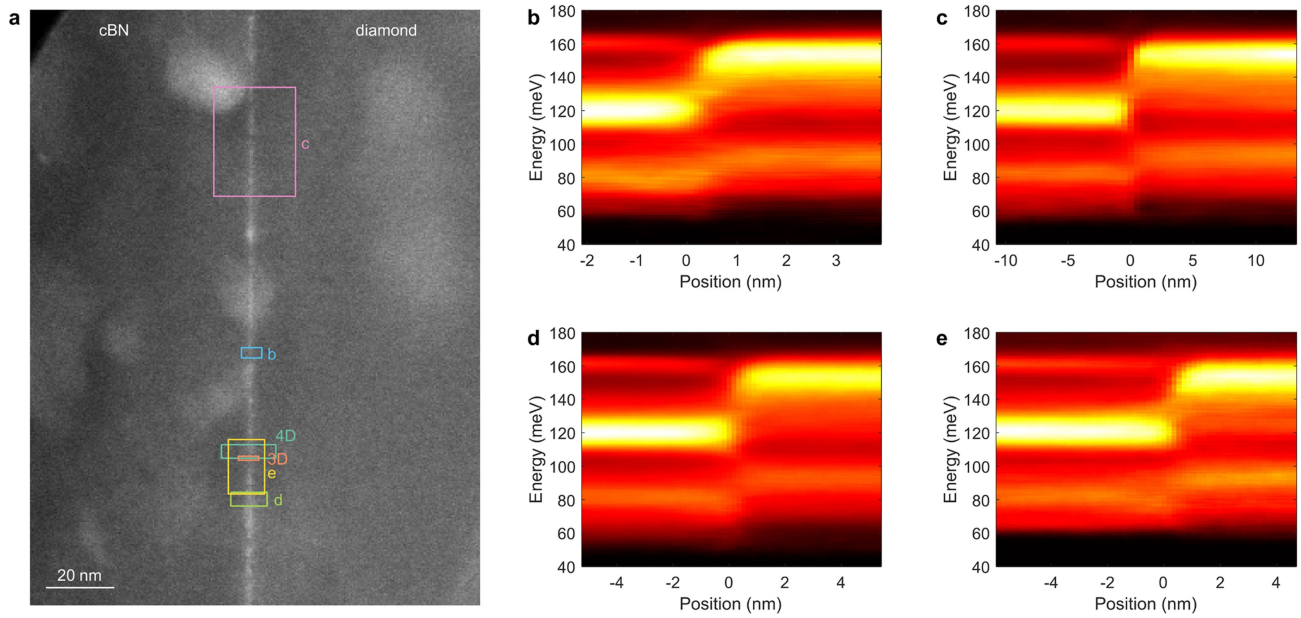


**Extended Data Fig. 3 | 3D EELS data acquired in different regions.** **a**, A low-magnification annular dark field image showing where the datasets were acquired. Boxes with labels '3D' and '4D' correspond to the scanning regions of the 3D EELS and 4D EELS datasets discussed in the main text. **b**–**e**, Four EELS line profiles acquired under the same experimental conditions except different pixel sizes and different scanning regions (marked in **a**). **b**, **c** and **d**, **e** were acquired in two experiments that were two weeks apart. All datasets give consistent results as the one shown in Fig. 2.

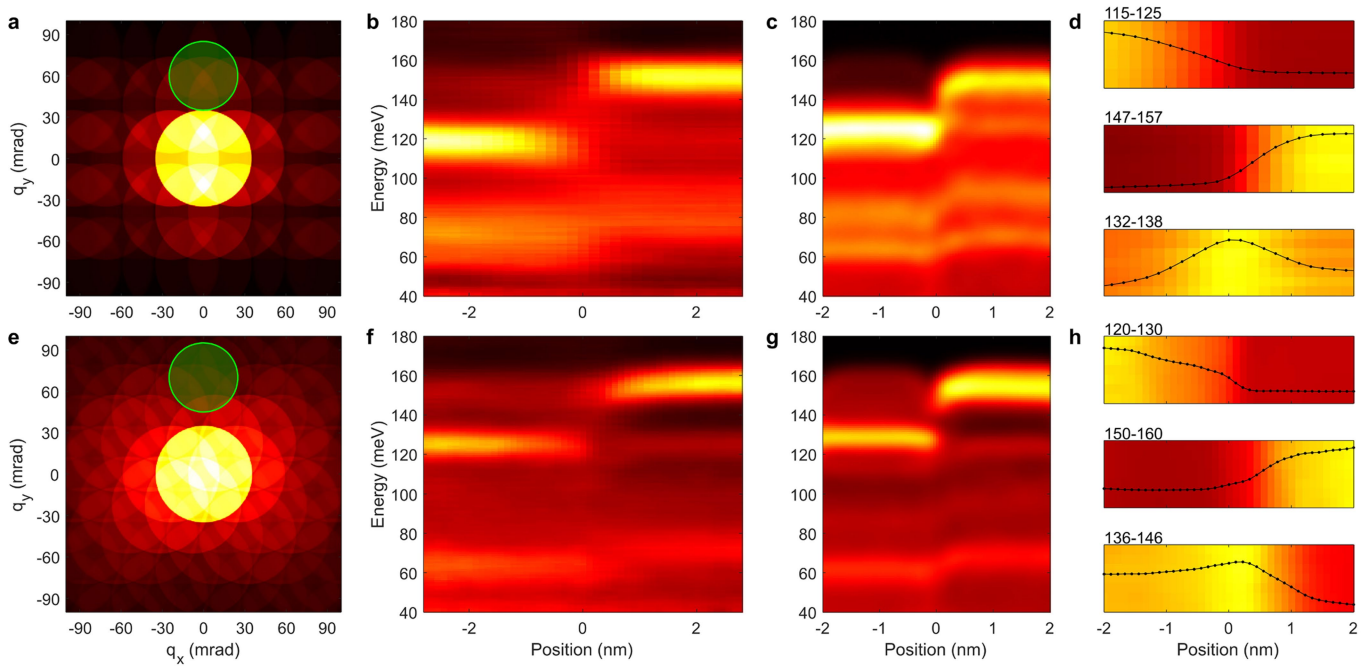


**Extended Data Fig. 4 | Off-axis EELS measurements. a**, A schematic of the diffraction plane and EELS aperture placement. The colormap illustrates the diffraction plane viewed from [11$\bar{2}$] zone axis, with 60 kV beam energy and 35 mrad convergence semi-angle. The diffraction spot size (35 mrad) is larger than the distance between adjacent spots, so they partially overlap. The green circle marks the position of the aperture, which is displaced away from the central spot. **b**, The EELS line profile acquired with off-axis geometry. Main spectral features are consistent with those acquired with on-axis geometry (Fig. 2b, Extended Data Fig. 3). **c**, Corresponding simulation result. **d**, EELS maps at selected energies. One of the interfacial modes has a better contrast than the on-axis result. **e**–**h**, same as **a**–**d**, but the beam is travelling along [1$\bar{1}$0] direction.

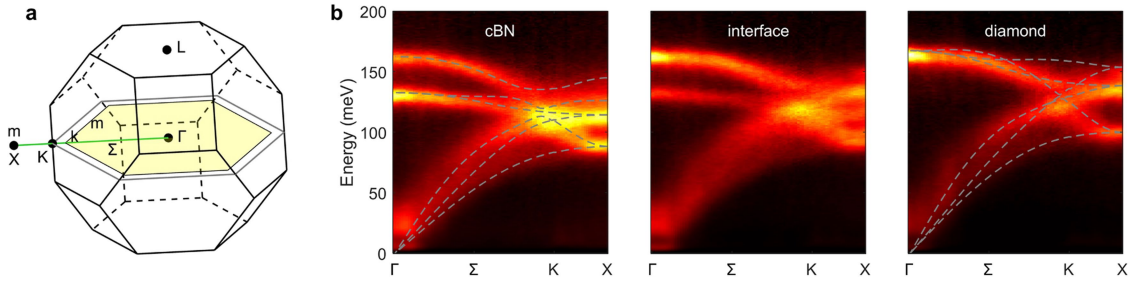


**Extended Data Fig. 5 | Phonon dispersion diagrams measured with 3 mrad convergence semi-angle. a**, A schematic of the bulk BZ (truncated octahedron) and the interface two-dimensional BZ (yellow hexagon). Upper-case and lower-case letters mark the high-symmetry points of the bulk BZ and interface BZ, respectively. **b**, Measured dispersion diagrams along the Γ–Σ–K–X line with 3 mrad convergence semi-angle. Dashed curves are calculated bulk phonon dispersion. Although smaller convergence semi-angles give better momentum resolution and hence nicer dispersion diagrams, insufficient spatial resolution makes it hard to extract localized features at the interface.

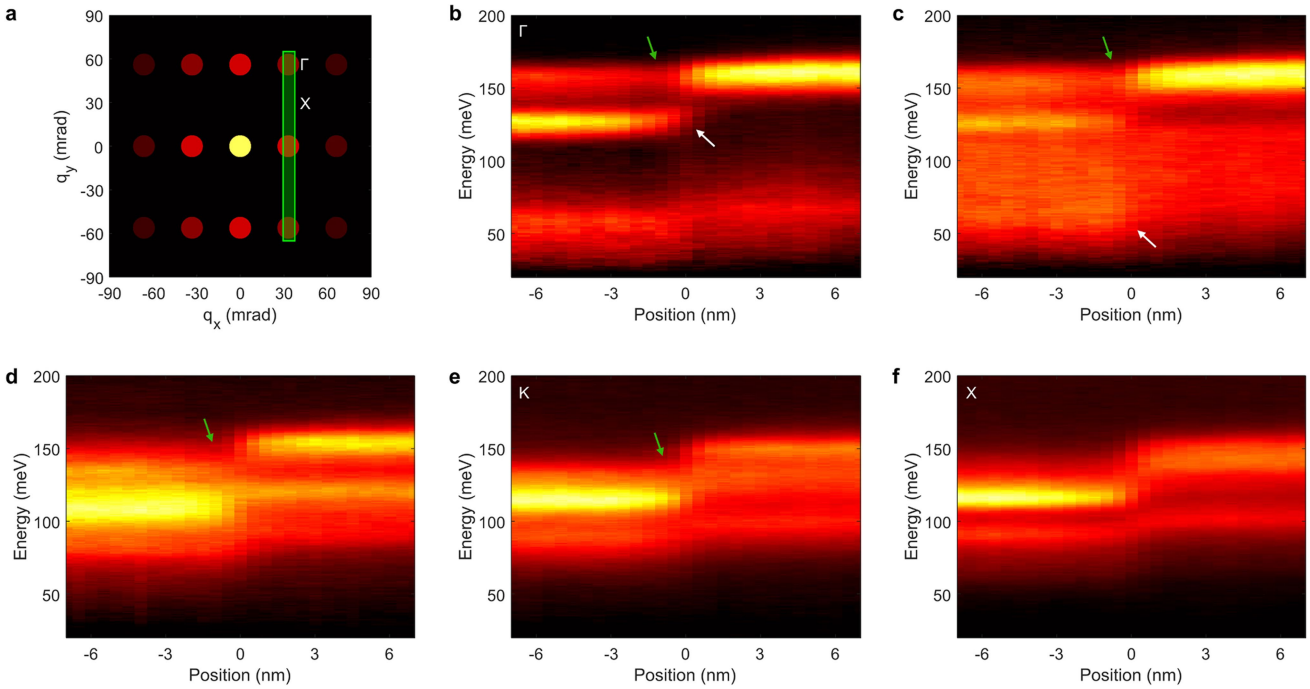


**Extended Data Fig. 6 | EELS line profiles at five momentum transfers.** **a**, A schematic of the diffraction plane and EELS aperture placement. The colormap illustrates the diffraction plane viewed from [11$\bar{2}$] zone axis, with 30 kV beam energy and 7.5 mrad convergence semi-angle. The diffraction spot size is drawn to scale, indicating our momentum resolution. The green rectangle marks the position of the slot aperture. **b**–**f**, Line profiles with momentum transfers from Γ (**b**) through the Σ line (**c**, **d**) to K (**e**) and finally X (**f**). The intensity decrease of the highest-frequency optical phonon is observable in most panels (green arrows), which corresponds to the negative-intensity line at 150-160 meV in Fig. 3c, d. The interfacial mode is directly observable in some panels (white arrows).

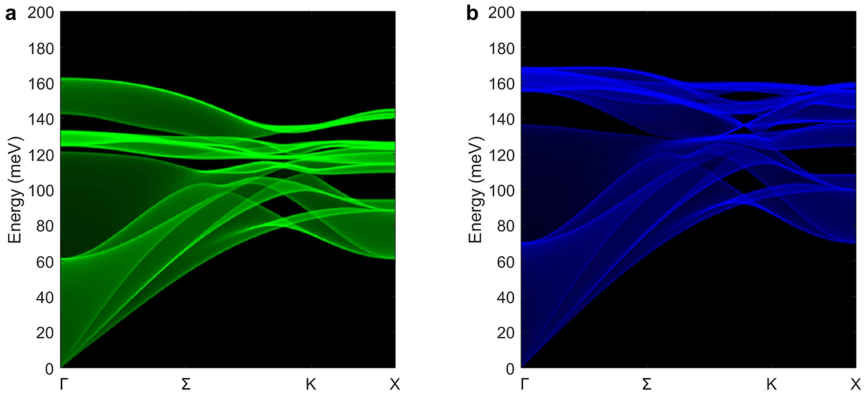


**Extended Data Fig. 7 | Projected bulk phonon bands. a**, **b**, Bulk phonon band of cBN and diamond projected onto (111) surface.

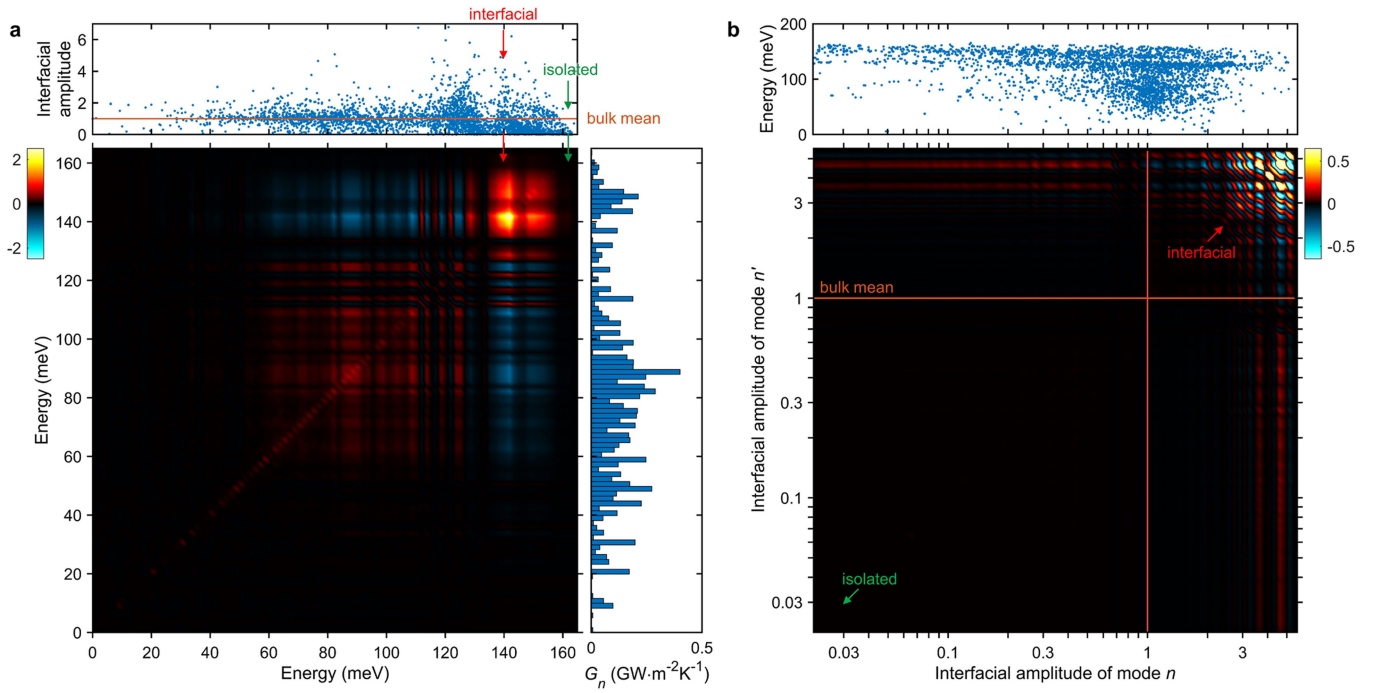


**Extended Data Fig. 8 | Modal contribution to ITC. a**, ITC decomposed into the mode-mode correlation integrals (Methods), with modes binned by their frequency. 8640 eigen modes are divided into 100 frequency bins. Main panel, pseudo-colour map of ITC component $G_{nn'}$ from heat flux correlation between $n$th and $n'$th frequency bin. Colour scale is in units of GW m$^{-2}$K$^{-1}$. Qualitatively it gives a measure of how strong two modes interact with each other. Right panel shows modal thermal conductance $G_n$ in the $n$th frequency bin, i.e., projecting the $G_{nn'}$ map along one dimension. Top panel is a scatter plot showing the frequency versus interface vibration amplitude for each eigen mode. Interfacial modes show strong correlation with almost all other modes (red arrows), while isolated modes have almost no correlation with any other modes (green arrow) **b**, ITC decomposed into the mode-mode correlation integrals, with modes sorted by their interfacial amplitudes. The same set of eigen modes are sorted by their amplitudes at the interface, aiming to visualize the relation between interfacial amplitudes and modal thermal conductance. For clarity, eigenvectors are normalized such that the squared norm of each eigenvector is the number of atoms (this is just an overall scaling of all eigenvectors), so an interfacial amplitude greater than one means an enhanced vibration at the interface and a value smaller than one means a reduced vibration at the interface. Main panel shows the per-mode (i.e., divided by the number of modes in each bin) contribution to ITC from the modal heat flux correlation between $n$th and $n'$th amplitude bin. Colour scale is in units of MW m$^{-2}$K$^{-1}$. Modes with enhanced amplitudes at the interface show strong correlation with all other modes, while modes with reduced amplitudes at the interface show little correlation with other modes. Top panel gives the scatter plot of frequency versus interfacial amplitude again.

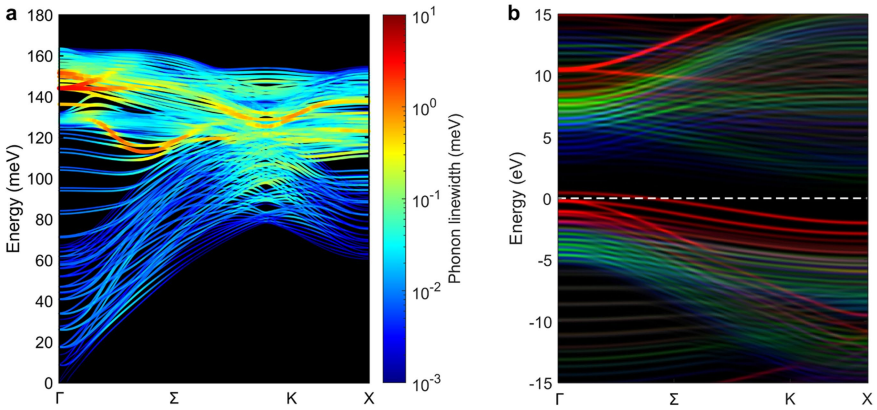


**Extended Data Fig. 9 | Electron-phonon coupling at the interface calculated by DFPT. a**, Phonon linewidth due to electron-phonon coupling mapped on the phonon dispersion. Compared with bulk modes, the interfacial optical modes couple strongly with electrons (note that the colour map is in log scale) because both the interfacial phonon modes and the two-dimensional electron gas are highly confined at the interface. **b**, Electronic band structure. Three RGB channels represent electron wavefunctions projected onto atomic orbitals in the interface region (red), in cBN (green) and in diamond (blue). Dashed horizontal line is the Fermi level, which crosses a band localized near the interface, meaning the system becomes metallic due to carriers at the interface.